9th IAA Planetary Defense Conference – PDC 2025
5–9 May 2025, Stellenbosch, Cape Town, South Africa

IAA-PDC25-06-16

Optimizing Trajectories in Asteroid Defense Missions: Potential Gains from Eccentric Collision Approaches

Kinthong Lee[a,1], Hexi Baoyin[a,2], Zhaokui Wang[a,3,*]

[a]School of aerospace engineering Tsinghua University, 30 Shuangqing Rd, Haidian District, Beijing, 100160, China

Abstract

In asteroid deflection missions, the presence of ejecta leads to a phenomenon where the system's momentum appears to be "amplified." This effect can be leveraged; By utilizing an eccentric strike strategy, the deflection distance can be further magnified compared to a direct center-of-geometry collision. In traditional trajectory optimization, in order to maximize the deflection distance, the optimal transfer trajectory usually ends with the velocity of the spacecraft and asteroid being parallel, which, in other words, the interception angle is as close to zero as possible. This paper predicts that by introducing the eccentric strike strategy into the optimizer, this limitation will be significantly loosened, allowing the optimizer to explore a trajectory with larger intercept angles, which could not be found by the traditional optimizer, thereby achieving larger deflection distances. In this study, we performed deflection simulations on 32 potentially hazardous asteroids (PHAs) to validate this claim. The results indicate that, for all PHAs tested, the eccentric collision strategy achieves higher deflection distances than the traditional approach, with an average improvement of 38.61%. In most cases, the intercept angles derived are notably larger than those obtained via the traditional method. Furthermore, for certain specific PHAs, the conventional method fails to produce a positive deflection distance, whereas the eccentric collision approach successfully finds an intercept trajectory that yields a positive deflection. This conclusion provides important theoretical support and technical groundwork for future asteroid defense strategies.

Keywords: Trajectory Optimization, Kinetic Deflection, Eccentric collision, Potential Hazardous Asteroid, Astrodynamic

1. Introduction

Asteroid impacts on Earth are considered to pose a significant threat to humanity. Currently, asteroids with diameters greater than one kilometer in the solar system have been largely discovered, and no objects posing a severe threat to Earth have been identified. However, although the probability of an asteroid with a diameter in the hundreds of meters range impacting Earth is relatively low, it is not zero. Although it is difficult to accurately estimate the number of asteroid impact events in Earth's history with current technology, approximately 170 confirmed meteorite craters worldwide suggest that asteroid impacts have occurred frequently. The most famous of these is the Chicxulub crater located on the Yucatán Peninsula, which has a diameter of 198 kilometers and was formed 65 million years ago by an asteroid approximately 10 kilometers in diameter. This impact is widely believed to have been the main cause of the dinosaur extinction event[1].

*Corresponding author
Email addresses: lijintan23@mails.tsinghua.edu.cn (Kinthong Lee), baoyin@tsinghua.edu.cn (Hexi Baoyin), wangzk@tsinghua.edu.cn (Zhaokui Wang)
[1]Master Student, School of Aerospace Engineering Tsinghua University
[2]Professor, School of Aerospace Engineering Tsinghua University; also Inner Mongolia Uni versity of Technology
[3]Professor, School of Aerospace Engineering Tsinghua University

With sufficient warning, humanity can employ various deflection strategies to alter the trajectory of these hazardous objects, thus averting potential collisions with Earth[2]. Including kinetic deflection method[3, 4, 5], ion beam shepherd method[6, 7], nuclear explosion[8, 9], etc. Within the current framework, kinetic impact technology is considered the most feasible countermeasure for medium-sized objects with a warning time of 10 to 20 years, due to its relatively high level of maturity. This approach is particularly emphasized in the Double Asteroid Redirection Test (DART), a collaborative effort between the National Aeronautics and Space Administration (NASA) and the European Space Agency (ESA)[10, 11, 12]. Cheng et al., through their analysis of data from the DART mission, discovered that the momentum transferred to the Didymos-Dimorphos asteroid system after the collision appeared to be "amplified" by a factor of 3.61[13]. This phenomenon of momentum amplification is primarily attributed to the recoil effect of the ejected material generated during the high-speed collision.

Lee et al. further exploited this phenomenon and proposed an eccentric striking strategy, known as the Best Impact Point (BIP). Which differs from most of the existing research, which has primarily focused on impacts along the center of geometry (COG) of the asteroid. This eccentric impact method can achieve a greater deflection distance between the asteroid and Earth, compared to striking through the Center of Geometry (COG), while maintaining all other collision parameters constant[3]. They conducted deflection simulation experiments on 32 potentially hazardous asteroids (PHAs) and demonstrated that the BIP strategy could achieve an average deflection distance that is 81% higher than that obtained using the COG strategy. The study employed the most fundamental type of transfer trajectory, namely the bi-impulse transfer, also known as the Lambert transfer. The COG strategy was initially used for preliminary screening to identify the optimal transfer trajectory. The BIP strategy was then introduced and compared on this transfer trajectory. However, the transfer trajectories identified by this approach typically have relatively small intercept angles α. However, their simulation results revealed a key statistical trend: as the interception angle gradually increases, the BIP strategy exhibits an increasingly advantageous effect compared to the COG strategy.

For impulsive low-thrust combined transfer trajectories, which align more closely with actual space missions, traditional trajectory optimization methods often tend to identify an optimal transfer trajectory with an interception angle α approaching as small as possible. In other words, the optimization process usually aims to make the velocity vector of the spacecraft $\mathbf{v}_{\text{spc}}$ as close as possible to the parallel with the velocity of the PHA $\mathbf{v}_{\text{PHA}}$ at the time of impact. This configuration maximizes the projection of the PHA's post-impact velocity change $\delta\mathbf{v}_{\text{PHA}}$ along the direction of its velocity, expressed as $\max(\text{proj}_{\mathbf{v}_{\text{PHA}}}\delta\mathbf{v}_{\text{PHA}})$, thus maximizing the deflection distance[14].

This study claims that by introducing an eccentric impact strategy into trajectory optimization considerations, the constraint of the interception angle α being small will be substantially loosened. This adjustment allows the optimization process to explore a trajectory with larger intercept angles α, which could not be found by the traditional optimizer, thus achieving larger deflection distances. To validate this hypothesis, the study employs a transfer trajectory that combines impulsive and low-thrust maneuvers, using 32 potentially hazardous asteroids (PHAs) as the target for deflection simulation. A particle swarm optimization (PSO) algorithm is utilized for trajectory optimization. A comparative analysis of the two approaches (COG and BIP strategies) will be conducted to verify the feasibility of eccentric impact strategies in planetary defense missions. It is predicted that for each simulation of every PHA, there exists a transfer trajectory with a larger interception angle α and strike at BIP, resulting in a deflection distance superior to that of the traditional approach with a near-zero interception angle and strike at the COG.

2. Modeling

2.1. Collision Model

In our earlier work[3] (Lee et al.), we carried out a comprehensive derivation of hypervelocity collision phenomena relevant to planetary defense. For completeness, we now provide a concise re-derivation of those results.

Figure 1 presents a schematic of a collision between a spacecraft and a PHA. In a hyper-velocity impact scenario, fragments from the PHA's surface can attain velocities exceeding the PHA's escape velocity, depart while carrying momentum from the PHA. This is called the ejecta phenomenon $\beta > 1$.

According to the Conservation of Momentum:

$$M\mathbf{v}_{\text{PHA}} + m\mathbf{v}_{\text{spc}} = \left(M + m - \sum m^*\right)\mathbf{v}'_{\text{PHA}} + \mathbf{P}_{\text{ej}} \tag{1}$$

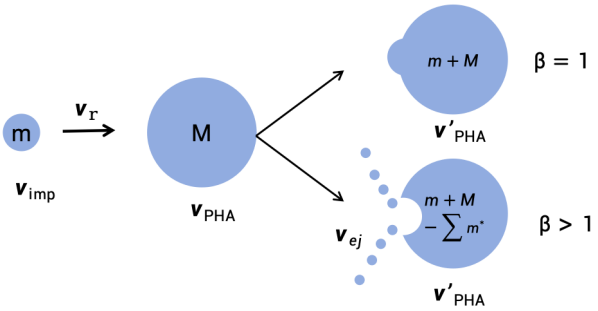

Figure 1: Schematic Diagram of the Collision Process Between a Spacecraft and a Small Celestial Body.

Where $\mathbf{P}_{\text{ej}}$ denotes the momentum of the ejecta resulting from the impact. The term $\sum m^*$represents the aggregate mass of the ejecta. The variable m represents the mass of the spacecraft, while M corresponds to the mass of the PHA. $\mathbf{v}_{\text{PHA}}$ refers to the pre-impact velocity vector of the PHA, $\mathbf{v}_{\text{spc}}$ to the pre-impact velocity vector of the spacecraft, and $\mathbf{v}'_{\text{PHA}}$ to the post-impact velocity vector of the PHA

Given that $\sum m^* \ll M + m$, yielding:

$$M\left(\mathbf{v}'_{\text{PHA}} - \mathbf{v}_{\text{PHA}}\right) = -\mathbf{P}_{\text{ej}} + m\left(\mathbf{v}_{\text{spc}} - \mathbf{v}'_{\text{PHA}}\right) \tag{2}$$

$$M\delta\mathbf{v} = -\mathbf{P}_{ej} + m\mathbf{v}_{\text{r}} \tag{3}$$

Where $\delta\mathbf{v} = \mathbf{v}'_{\text{PHA}} - \mathbf{v}_{\text{PHA}}$ represents the change in velocity vector of the PHA, and $\mathbf{v}_{\text{r}} = \mathbf{v}_{\text{spc}} - \mathbf{v}_{\text{PHA}} \approx \mathbf{v}_{\text{spc}} - \mathbf{v}'_{\text{PHA}}$ denotes the relative velocity vector of the spacecraft with respect to the PHA.

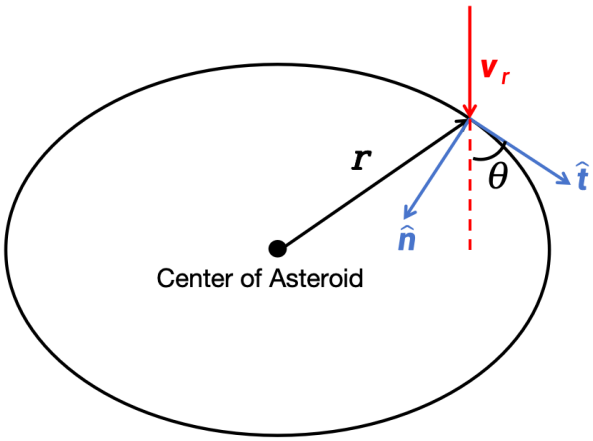

Figure 2: Schematic of a spacecraft impacting the surface of an asteroid.

When striking a specific surface of the PHA, construct two unit vectors $\hat{\mathbf{n}}$ and $\hat{\mathbf{t}}$, where represent the inward surface normal unit vector and downrange directed surface tangent unit vector as illustrated in Fig. 2

Project Eq.(3) onto the normal direction unit vector $\hat{\mathbf{n}}$:

$$M\delta\mathbf{v} \cdot \hat{\mathbf{n}} = -\mathbf{P}_{ej} \cdot \hat{\mathbf{n}} + m\mathbf{v}_{\text{r}} \cdot \hat{\mathbf{n}} \tag{4}$$

$$\delta\mathbf{v} \cdot \hat{\mathbf{n}} = \frac{-\mathbf{P}_{\text{ej}} \cdot \hat{\mathbf{n}} + m\mathbf{v}_{\text{r}} \cdot \hat{\mathbf{n}}}{M} \tag{5}$$

$$\delta\mathbf{v} \cdot \hat{\mathbf{n}} = \frac{-\mathbf{P}_{\text{ej}} \cdot \hat{\mathbf{n}} + m\mathbf{v}_{\text{r}} \cdot \hat{\mathbf{n}}}{m\mathbf{v}_{\text{r}} \cdot \hat{\mathbf{n}}} \cdot \frac{m\mathbf{v}_{\text{r}} \cdot \hat{\mathbf{n}}}{M} \tag{6}$$

Define the normal momentum transfer coefficient β as:

$$\beta = \frac{-\mathbf{P}_{\text{ej}} \cdot \hat{\mathbf{n}} + m\mathbf{v}_{\text{r}} \cdot \hat{\mathbf{n}}}{m\mathbf{v}_{\text{r}} \cdot \hat{\mathbf{n}}} = 1 + \frac{-\mathbf{P}_{\text{ej}} \cdot \hat{\mathbf{n}}}{m\mathbf{v}_{\text{r}} \cdot \hat{\mathbf{n}}} \tag{7}$$

we have:

$$\delta \mathbf{v} \cdot \hat{\mathbf{n}} = \beta \frac{m \mathbf{v}_{\mathrm{r}} \cdot \hat{\mathbf{n}}}{M} \tag{8}$$

Similarly, projecting Eq.3 onto the unit vector in the tangential direction $\hat{\mathbf{t}}$, we have:

$$\delta \mathbf{v} \cdot \hat{t} = \gamma \frac{m \mathbf{v}_{\mathrm{r}} \cdot \hat{t}}{M} \tag{9}$$

Where γ represents the tangential momentum transfer coefficient:

$$\gamma = 1 + \frac{-\mathbf{P}_{\mathrm{ej}} \cdot \hat{\mathbf{t}}}{m \mathbf{v}_{\mathrm{r}} \cdot \hat{\mathbf{t}}} \tag{10}$$

Therefore, Eqn.(3) can be expressed using β and γ:

$$\delta \mathbf{v} = (\delta \mathbf{v} \cdot \hat{n}) \hat{n} + (\delta \mathbf{v} \cdot \hat{t}) \hat{t} \tag{11}$$

$$\delta \mathbf{v} = \frac{m}{M} \left[\beta \left(\mathbf{v}_{\mathrm{r}} \cdot \hat{\mathbf{n}} \right) \hat{\mathbf{n}} + \gamma \left(\mathbf{v}_{\mathrm{r}} \cdot \hat{\mathbf{t}} \right) \hat{\mathbf{t}} \right] \tag{12}$$

Raducan et al. conducted an analysis of oblique impacts similar to the DART mission using the iSALE 3D simulation [15], Lee et al. analyzed their results[3] and fitted a relationship between β, γ, and the impact angle θ:

$$\gamma = 1 + (\beta - 1) \tan(\theta) \tan\left(-0.0052\theta^2 + 1.3629\theta - 80.871 \right) \tag{13}$$

Cheng et al. conducted a study on variations in Dimorphos orbital elements after the impact of the DART mission, presenting an interval for the beta coefficient $\beta = 3.61^{+0.19}_{-0.25}(1\sigma)$[13]. Several laboratory experiments have observed that the value of β is affected by the impact angles θ [16, 17]. The work of S.D. Raducan et al., using iSALE-3D simulations of DART-like impacts at oblique angles, show that as the impact angle θ decreases from 90° to 30°, the variation in β is less than 3.5%.[15]. Therefore, in the model presented in this study, β is fixed at 3.61. Once the spacecraft's intercept trajectory is determined, θ can be confirmed through Eqn.(14). Thus the tangential momentum transfer coefficient γ can be calculated with Eqn.(13).

$$\theta = \cos^{-1}\left(\frac{\mathbf{v}_{\mathrm{spc}} \cdot \mathbf{v}_{\mathrm{PHA}}}{\|\mathbf{v}_{\mathrm{spc}}\| \|\mathbf{v}_{\mathrm{PHA}}\|} \right) \tag{14}$$

With given three-dimensional model of Apophis, obtained using the light curve inversion technique[18], allows the determination of $\left(\hat{\mathbf{n}}, \hat{\mathbf{t}}, \theta\right)$. By using Eqn.(12), the $\delta \mathbf{v}$ generated by striking each geometric surface of the asteroid can be calculated.

For a kinetic deflection mission in which the duration between the impact date and the PHA's close-approach (CA) date with Earth exceeds half of the PHA's heliocentric orbital period, the impulse direction along the PHA's orbital velocity $\hat{\mathbf{v}}_t$ is the most effective strategy to increase the minimum orbit intercept distance (MOID) with Earth [14]. The curve $\gamma - \theta$ for different values of β derived from Eqn.(13), is plotted in Fig.(3). It is evident that the normal momentum transfer coefficient β is always several times higher than the tangential momentum transfer coefficient γ. Therefore, it can be expected that when the spacecraft velocity is not parallel to the asteroid's velocity, impacting geometric points on the asteroid rather than the geometric center can further amplify the component of the normal ejecta momentum in the direction of the asteroid's velocity. Fig.(4) illustrates the schematic of this theory, under the same intercept angle condition $\alpha = 60^\circ$, it is clear that $\mathrm{proj}_{\mathbf{v}_{\mathrm{ast}}} \mathbf{P}_{\mathrm{ej,n}}$ generated by BIP (red) is larger than COG (blue).

This phenomenon is quite similar to playing snooker, except that in this scenario, ejecta are an additional factor.

2.2. Optimization Method

This optimization problem deviates from the conventional Bolza type. While many space trajectory problems typically involve straightforward objectives, such as minimizing flight time or maximizing final mass, this case does not allow for an explicit expression of the objective function, such as a function of states or a path-dependent integral. Instead, the objective is to maximize the deflection achieved, specifically by maximizing the perigee altitude during the asteroid's Earth flyby, which is complex to calculate.

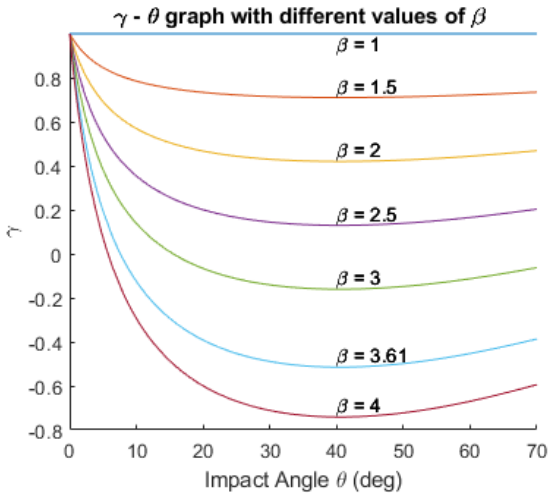

Figure 3: $\gamma - \theta$ curve for different values of β.

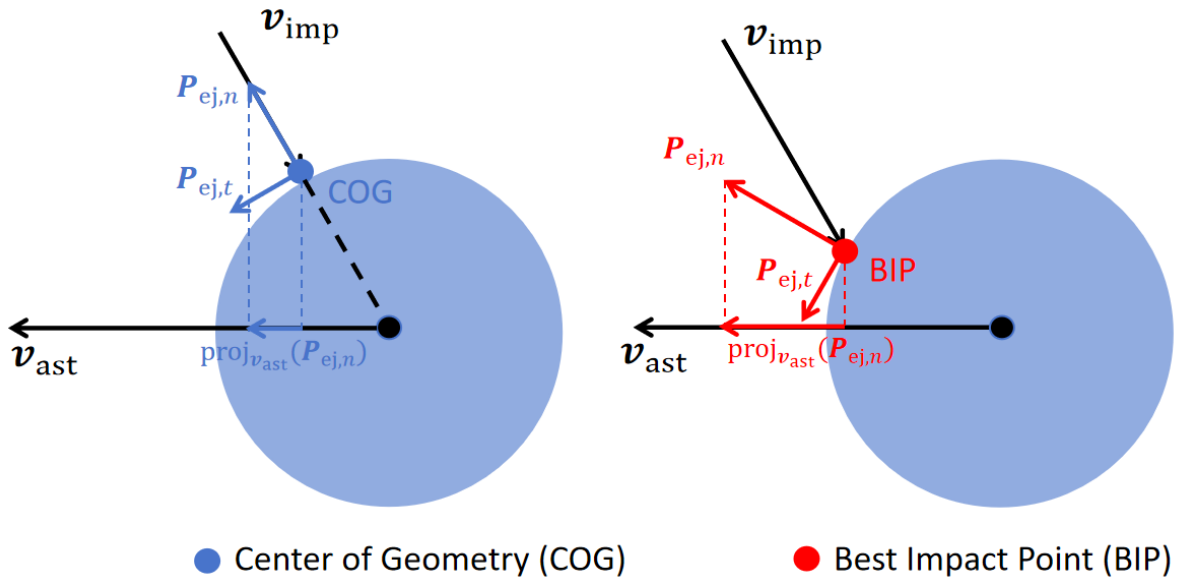

Figure 4: Schematic diagram of different impact point under same impact angle $\theta = 60°$. The BIP strategy yeilds a higher $\text{proj}_{\mathbf{v}_{\text{ast}}} \delta\mathbf{v}$ than COG strategy

2.2.1. Calculating the Deflection Distance

Inspired by the work of Conway et al. [19] and with some modifications, the process for calculating the deflection distance of the PHA is illustrated in Fig.(5). Specifically, this process can be divided into the following seven steps to determine the deflection distance.

1. Earth Departure Phase: Since this study primarily focuses on the gain of eccentric impacts for planetary defense rather than simulating an actual deep space mission, an idealized launch model is employed during the launch phase. Specifically, at the launch moment, it is assumed that the spacecraft's position vector coincides with the Earth's position vector (in the heliocentric J2000 coordinate system), and the influence of Earth's gravity is neglected. This simplification method is widely used in early mission planning to quickly assess the feasibility of different launch windows and transfer orbits. The optimizer gives the launch date t_{launch}, the velocity magnitude generated by the impulse ΔV, as well as the right ascension (RA) and the declination (DEC). After applying the impulse, the spacecraft's state is:

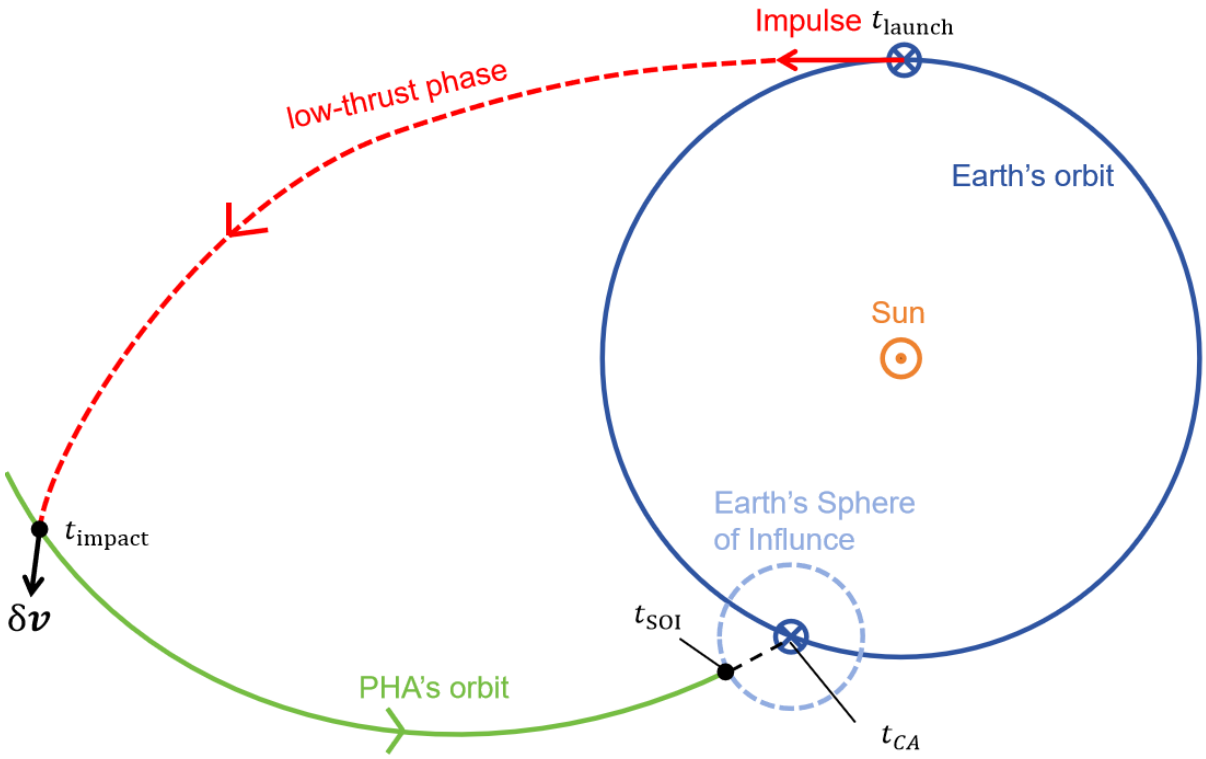

Figure 5: Steps to calculate deflection distance.

$$\begin{cases} \mathbf{r}_{\text{spc}}\left(t_{\text{launch}}\right) = \mathbf{r}_{\text{Earth}}\left(t_{\text{launch}}\right) \\ \mathbf{v}_{\text{spc}}\left(t_{\text{launch}}\right) = \mathbf{v}_{\text{Earth}}\left(t_{\text{launch}}\right) + \Delta V \mathbf{R} \begin{bmatrix} \cos(\text{DEC})\cos(\text{RA}) \\ \cos(\text{DEC})\sin(\text{RA}) \\ \sin(\text{DEC}) \end{bmatrix} \end{cases} \tag{15}$$

Where $\mathbf{R}$ represents the transformation matrix from the Geocentric Equatorial Coordinate System to the heliocentric J2000 coordinate system:

$$\begin{gathered} \mathbf{R} = \begin{bmatrix} \hat{\mathbf{r}}_{\text{Earth}} & \hat{\mathbf{t}}_{\text{Earth}} & \hat{\mathbf{h}}_{\text{Earth}} \end{bmatrix} \\ \hat{\mathbf{r}}_{\text{Earth}} = \frac{\mathbf{r}_{\text{Earth}}}{r_{\text{Earth}}}, \hat{\mathbf{t}}_{\text{Earth}} = \hat{\mathbf{h}}_{\text{Earth}} \times \hat{\mathbf{r}}_{\text{Earth}}, \hat{\mathbf{h}}_{\text{Earth}} = \frac{\mathbf{r}_{\text{Earth}} \times \mathbf{v}_{\text{Earth}}}{r_{\text{Earth}}\, v_{\text{Earth}}} \end{gathered} \tag{16}$$

2. Following escape from Earth, low-thrust propulsion is employed. Under heliocentric J2000 coordinate system, the corresponding dynamical equation is expressed as:

$$\begin{aligned} \dot{x} &= v_x \\ \dot{y} &= v_y \\ \dot{z} &= v_z \\ \dot{v}_x &= -\frac{\mu}{r^3} x + a_{\text{LT},x} + a_{\text{p},x} \\ \dot{v}_y &= -\frac{\mu}{r^3} y + a_{\text{LT},y} + a_{\text{p},x} \\ \dot{v}_z &= -\frac{\mu}{r^3} z + a_{\text{LT},z} + a_{\text{p},z} \end{aligned} \tag{17}$$

Where:

$$\begin{aligned} a_{\text{LT},x} =& \frac{a_{\text{LT}}(t) x}{r} \sin(\theta_{\parallel}) \cos(\theta_{\perp}) + \frac{a_{\text{LT}}(t)}{r^2 v} \left[\left(z^2 + y^2\right) v_x - x\left(z v_z + y v_y\right)\right] \cos(\theta_{\parallel}) \cos(\theta_{\perp}) \\ &+ \frac{a_{\text{LT}}(t)}{rv} \left[y v_z - z v_y\right] \sin(\theta_{\perp}) \\ a_{\text{LT},y} =& \frac{a_{\text{LT}}(t) y}{r} \sin(\theta_{\parallel}) \cos(\theta_{\perp}) + \frac{a_{\text{LT}}(t)}{r^2 v} \left[\left(x^2 + z^2\right) v_y - y\left(x v_x + z v_z\right)\right] \cos(\theta_{\parallel}) \cos(\theta_{\perp}) \\ &+ \frac{a_{\text{LT}}(t)}{rv} \left[z v_x - x v_z\right] \sin(\theta_{\perp}) \\ a_{\text{LT},z} =& \frac{a_{\text{LT}}(t) z}{r} \sin(\theta_{\parallel}) \cos(\theta_{\perp}) + \frac{a_{\text{LT}}(t)}{r^2 v} \left[\left(y^2 + x^2\right) v_z - z\left(y v_y + x v_x\right)\right] \cos(\theta_{\parallel}) \cos(\theta_{\perp}) \\ &+ \frac{a_{\text{LT}}(t)}{rv} \left[x v_y - y v_x\right] \sin(\theta_{\perp}) \end{aligned} \tag{18}$$

Where μ is the gravitational parameter of the Sun, $a_{\text{LT}}(t) = \frac{c n_0}{c - n_0 t}$ is the low-thrust accerelation generated by the engine, c and n_0 represent exhaust velocity and initial thrust-to-mass ratio generated by the low-thrust engine, $(\theta_{\parallel}, \theta_{\perp})$ represents the in-plane and out-of-plane pointing angle by the low-thrust engine. The a_{p} are perturbations from Venus, Mars, Jupiter, and Solar radiation pressure.

3. At the impact date t_{impact} given by the optimizer, the difference between the spacecraft's position vector and PHA's position vector must be on the order of 10^0 m or less, indicating a collision. The position vector of PHA can be obtained from the DE441 ephemeris.

4. After the collision, the velocity vector of the PHA undergoes a slight change. At this point, the process branches into two paths, utilizing the COG and BIP impact strategies, respectively. The resulting $\delta\mathbf{v}$ from both strategies can be calculated by Eqn.(12), which has been discussed in detail in Section(2.1). The remaining mass of the spacecraft following the impulse and low-thrust acceleration is:

$$m(\Delta V, t_{\text{impact}} - t_{\text{launch}}) = m_0 \exp\left(-\frac{\Delta V}{c}\right) \exp\left(-\frac{n_0}{c}\left(t_{\text{impact}} - t_{\text{launch}}\right)\right) \tag{19}$$

Where the c represent the exhaust velocity of spacecraft's propulsion system, n_0 represents the spacecraft initial thrust acceleration,

The state of the PHA after the collision is:

$$\begin{cases} \mathbf{r}_{\text{PHA}}\left(t^{+}_{\text{impact}}\right) = \mathbf{r}_{\text{PHA}}\left(t^{-}_{\text{impact}}\right) \\ \mathbf{v}_{\text{PHA}}\left(t^{+}_{\text{impact}}\right) = \mathbf{v}_{\text{PHA}}\left(t^{-}_{\text{impact}}\right) + \delta\mathbf{v} \end{cases} \tag{20}$$

5. In heliocentric J2000 frame, a high-precision orbital propagator (HPOP) is employed to propagate PHA' state from the impact date t_{impact} until the moment the PHA enters Earth's sphere of influence (SOI) t_{SOI}. The considered perturbations include the gravitational influences of Venus, Earth, Moon, Mars, and Jupiter, as well as solar radiation pressure.

6. In geocentric J2000 frame, employs HPOP to propagate PHA' state from the t_{SOI} until one day after PHA' closest approach (CA) to Earth. The minimum value of the magnitude of the PHA's position vector in the geocentric coordinate system corresponds to PHA' perigee altitude to Earth.

The process yields a CA distance of 38,010 km when Apophis is not deflected, which matches the value provided in the JPL Small-Body Database.

2.2.2. Trajectory Optimization

Particle swarm optimization (PSO) is a heuristic numerical optimization method[19, 20, 21, 22, 23], it mimics the unpredictable motion patterns of bird flocks searching for food, employing an information-sharing mechanism to influence the overall behavior of the swarm. Specifically, the movement of each particle in the search space is influenced not only by its own historically best position, but also by the best position found by other particles in the swarm. This communication mechanism enables the particle swarm to dynamically adjust its search direction and velocity, thereby efficiently exploring the solution space and converging toward the global optimum. By emulating the intelligent behavior observed in natural biological swarms, PSO achieves efficient search performance in complex optimization problems while maintaining its simplicity and ease of use.

At the same time, among the various algorithms available, PSO is particularly well suited for this trajectory optimization problem. Because PSO requires a source of stochasticity in its process, and given the findings of Lee et al.[3], which demonstrate that the PHA attitude strongly influences collision-induced $\delta\mathbf{v}$, the fact that almost all PHAs lack a well-defined attitude effectively provides the randomness that PSO needs. A detailed discussion of this phenomenon is presented later in Section (3.2).

At initialization, the particles are randomly inserted into the search space. Unlike genetic algorithms, PSO does not discard poorly performing solutions; instead, all particles continuously traverse the search space to improve their objective values. During each iteration, the particles exchange their individual cost values with the entire swarm, which guides each particle's movement - incorporating both stochastic and inertial effects - toward the best known position of the group.

As an optimizer, PSO offers several advantages. Its implementation is straightforward and does not require the fulfillment of the necessary conditions of Pontryagin's maximum principle. Moreover, unlike non-linear programming (NLP) methods, PSO does not require an initial guess, which can be challenging (or even impossible) to generate and may bias the search toward a local region, and its iterative process is generally rapid.

However, the primary limitation of PSO is that the number of decision variables, n, must remain relatively small (typically less than 20) compared to NLP-based methods. Consequently, when defining variables, for example, for the continuous control required in low-thrust programs, using an NLP-based solver may involve hundreds or even thousands of decision parameters. Furthermore, PSO inherently lacks a built-in mechanism to incorporate equality or inequality constraints that depend on decision variables, in this case, at the time of impact, the difference between spacecraft and PHAs' position vectors approaches zero. In such cases, the constraint must be incorporated into the objective function via a penalty term.

The objective of the unconstrained particle swarm optimization problem is to determine the optimal values of the set of position parameters $\{\chi_1, \ldots, \chi_n\}$ that governed by the dynamic system, so that the objective function J is minimized. These n parameters are constrained within their respective bounds:

$$a_{\text{k}} \leq \chi_{\text{k}} \leq b_{\text{k}} \tag{21}$$

As discussed above, PSO is a swarm-based approach in which the swarm consists of N particles. Each particle $i\,(i = 1, \ldots, N)$ is associated with a position vector $\boldsymbol{\chi}(i)$ and a velocity vector $\mathbf{w}(i)$. It is important to note that, in this context, 'position' and 'velocity' refer to the parameter search space rather than the physical meaning. Each position vector $\boldsymbol{\chi}(i)$ and velocity vector $\mathbf{w}(i)$ encompasses the n unknown parameters of the problem:

$$\begin{aligned} \boldsymbol{\chi}(i) &= [\chi_1(i), \ldots, \chi_n(i)]^{\mathrm{T}} \\ \boldsymbol{w}(i) &= [w_1(i), \ldots, w_n(i)]^{\mathrm{T}} \end{aligned} \tag{22}$$

Both $\boldsymbol{\chi}(i)$ and $\mathbf{w}(i)$ are defined as n dimensional vectors. Since the position components are bounded, the corresponding velocity components must be restricted to an appropriate range to ensure that position updates do not cause particles to exceed their permissible domain.

Each particle represents a potential solution to the problem, corresponding to a specific value of the objective function J. The update expressions for position and velocity govern the evolution of the swarm toward the global optimal solution. The following outlines the steps for computing the objective function J in each generation:

1. for particle $i\,(i = 1, \ldots, N)$:

   a. Calculate the objective value for the particle $i\,(i = 1, \ldots, N)$, in current iteration j, denoted by $J^{(j)}(i)$.

   b. Identify the particle's personal best position up to the current iteration j, denoted as $\mathbf{y}^{(j)}(i)$.

   c. Determine the best global position, denoted as $\hat{\mathbf{y}}^{(j)}$, which is the position that yields the lowest objective function value among all particles up to the current iteration j.

2. Update the velocity vector: For each particle $i\,(i = 1, \ldots, N)$ and for each velocity component $w_k(i)\,(k = 1, \ldots, n)$, the value at iteration $j + 1$ is calculated as follows:

$$w_k^{(j+1)}(i) = c_{\mathrm{i}} w_k^{(j)}(i) + c_{\mathrm{c}} \left[y_k^{(j)}(i) - \chi_k^{(j)}(i) \right] + c_{\mathrm{s}} \left[\hat{y}_k^{(j)} - \chi_k^{(j)}(i) \right] \tag{23}$$

   Here, c_{i}, c_{c}, and c_{s} are weighting coefficients corresponding to the inertia, cognitive, and social, respectively. In low-thrust trajectory optimization, these parameters can be assigned the following values[19]:

$$c_{\mathrm{i}} = \frac{1 + r_1(0,1)}{2}, c_{\mathrm{c}} = 1.49445 r_2(0,1), \quad c_{\mathrm{s}} = 1.49445 r_3(0,1) \tag{24}$$

   where $r_1(0,1)$, $r_2(0,1)$, and $r_3(0,1)$ denote three independent random numbers, each uniformly distributed over the interval [0, 1].

3. Update the elements of the position vectors of all particles $(i = 1, \ldots, N)\,(k = 1, \ldots, n)$:

$$\chi_k^{(j+1)}(i) = \chi_k^{(j)}(i) + w_k^{(j+1)}(i) \tag{25}$$

In the experiments presented in this paper, the objective is to maximize the deflection distance of the PHAs. Consequently, the objective function J is defined as the negative of the deflection distance. All heuristic optimizers must employ a penalty function within the objective function to enforce the problem constraints. In this study, the constraint requires that the spacecraft collide with the PHAs at impact time t_{impact}. Consequently, the difference in their distances is multiplied by a penalty weight (which can be set to 100) and added to the objective function.

$$J = -\text{Deflection Distance} + 100 \left\| \boldsymbol{r}_{\text{spc}} \left(t_{\text{impact}} \right) - \boldsymbol{r}_{\text{PHA}} \left(t_{\text{impact}} \right) \right\| \tag{26}$$

The transfer trajectory found by PSO is usually not fully precise, often requiring further refinement using some direct optimization methods such as the Runge-Kutta Parallel Shooting (RKPS) approach. However, our team's extensive simulation results for nearly all PHAs indicate that the RKPS method is generally unable to further enhance the deflection distance achieved by PSO; the transfer trajectories identified by PSO are nearly optimal; this result is consistent with the findings reported by Conway et al.[19]. Therefore, the simulations in this study employ only PSO for trajectory optimization.

3. Simulation Setup

3.1. PSO parameters and Sequential Loops for PSO

As mentioned above, the PSO algorithm requires the parameter dimension to remain relatively modest, typically not exceeding $n \leq 20$. To this end, for the low-thrust phase, this study employs a fifth-order polynomial in transfer duration t_{TOF} to represent the in-plane angle $\theta_{\parallel}$ and the out-of-plane angle $\theta_{\perp}$. Thus, for the simulation of this problem, there are 17 PSO parameters: 12 low thrust angle polynomial coefficients, Earth departure magnitude ΔV, two Earth departure angles (RA, DEC), the launch date t_{launch} and impact date t_{impact}.

Based on our experience, the PSO algorithm for optimizing trajectories in planetary defense deflection missions tends to split into two phases: first stabilizes the "Deflection Distance" and then refining the "Interception Error", as indicated in Eqn.(26), the PSO objective function consists of two components: the Deflection Distance and the Interception Error. In the first 50 iterations, both components vary; however, from approximately the 50th iteration onward, the fluctuations in the Deflection Distance become minimal, suggesting that it no longer undergoes significant change and that the rest iterations focus primarily on reducing the Interception Error as shown in Fig.(6). Experience indicates that if, after about 50 iterations, the Deflection Distance remains at an unfavorable value (e.g., a negative value, meaning that the PHA being closer to Earth), then the algorithm is unable to escape this local optimum in subsequent iterations.

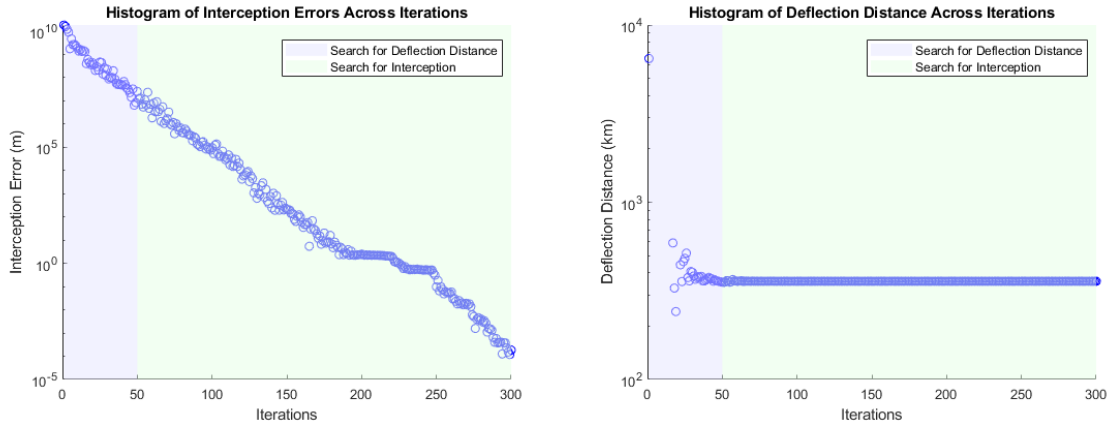

Figure 6: Histogram of Interception Error and Deflection Distance Over PSO Iterations, Showing the PSO algorithm tends to split into two phases: stabilizes the Deflection Distance first then refining the Interception Error

This phenomenon can be exploited for rapid preliminary screening. In our work, we employ a Sequential Loops approach to enhance simulation efficiency. In the first PSO loop, 20 particles and 50 iterations are used (experience shows that most of the times 20 iterations is enough for preliminary screening), and this PSO is repeated 200 times to fully explore the entire search space. The particle position χ with the best deflection distance obtained from these 200 runs is then used as a particle in the second loop of the PSO. In this second PSO loop, 200 particles and 300 iterations are executed in a single run. The results indicate that this Sequential Loops strategy substantially increases the efficiency of the PSO algorithm in identifying the global optimum. The flow chart is presented in Fig.(7).

3.2. Attitude of PHA 3D model

The work of Lee et al.[3] indicates that during collision, PHA $\delta\mathbf{v}$ is strongly correlated with the attitude of the PHA. Using a Monte Carlo approach, they generated 100,000 distinct attitudes for each PHA and obtained a frequency distribution of the resulting deflection distances. Their results show that, taking 99942 Apophis as an example, the deflection distance achieved by the COG strategy can vary by as much as 1,500 km due to attitude uncertainties, with a mean value of 923.59 km with $1\sigma = 273.29$ km, while the corresponding range for the BIP strategy is approximately 250 km, with a mean value of 1328.60 km and $1\sigma = 48.61$ km. However, upon closer examination, our team has observed that this attitude uncertainty fortuitously plays the same role as the three random weighting coefficients c_{i}, c_{c}, and c_{s} in the PSO algorithm, effectively dispersing the particles in an analogous manner. Consequently, the randomness introduced by attitude positively provides the stochasticity required by PSO.

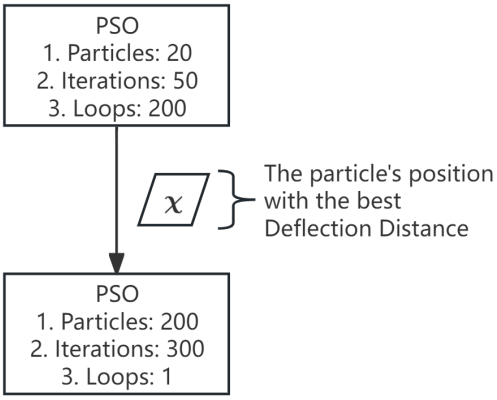

Figure 7: Flowchart of the Sequential Loops Approach for PSO: the first loop identifies the best deflection distance, and the second loop refines the interception error.

In this model, a 3D model derived from Apophis' lightcurve variations is employed for all PHAs[18]. At the moment of impact, a random attitude is generated for the collision calculation. Fig.(8) presents the heat map of $\text{proj}_{\mathbf{v}_{\text{ast}}}\delta\mathbf{v}$ generated by different impact surfaces with an intercept angle α of $5.22°$. The yellow area represents the impact surface with the largest $\text{proj}_{\mathbf{v}_{\text{ast}}}\delta\mathbf{v}$ which is selected as the impact sruface for BIP strategy, while the red area represents the impact surface passing through the geometric center, which is selected as COG strategy. It can be seen that these two areas do not overlap.

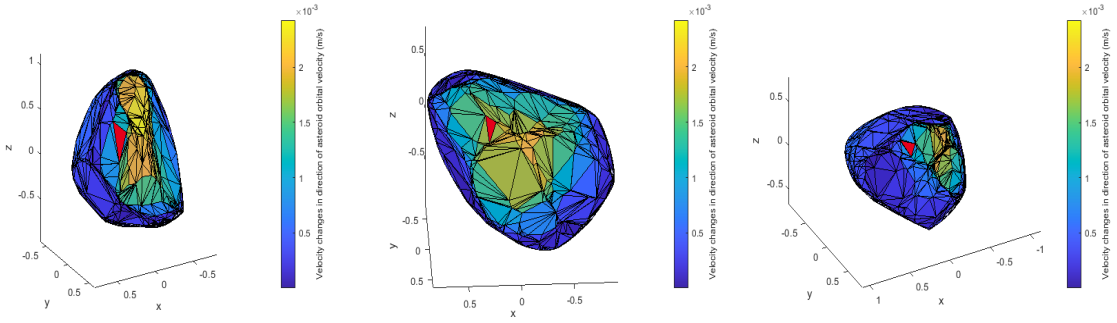

Figure 8: Impact an PHA at three different attitudes, with Interception Angle $\alpha = 5.22°$, represented as a heatmap showing the components of velocity change along the direction of PHA's orbital velocity $\text{proj}_{\mathbf{v}_{\text{ast}}}\delta\mathbf{v}$ (ms^{-1}). Red facets represents impact through PHA's COG

It should be emphasized that the 3D models presented here primarily represent the surface topology of the PHA on a large scale, far exceeding the dimensions of the impactor. However, results from the DART mission have shown that surface features comparable in size to the impactor, such as large rocks or mounds, can significantly influence the ejecta produced after impact, potentially causing the ejecta to completely deflect to one side of the impact site[24, 25, 26]. However, the purpose of this paper is to compare the results of the BIP and COG strategies. Thus, this study focuses solely on the influence of large-scale surface characteristics, leaving the detailed study of smaller-scale effects for future research.

3.3. Parameters for launch vehicle and PHAs

The parameters for the spacecraft and the low-thrust propulsion system are listed in Table (1).

This paper selects 32 PHAs from the NASA JPL CNEOS database[27] sorted by rarity in descending order as hypothetical defense targets. To facilitate better lateral comparisons, the mass of all PHAs is fixed at 2.7×10^{10} kg, as well as the 3D shape model of 99942 Apophis. The parameters of 32 PHAs are listed in Table (2).

sectionResult The analysis presented here is conducted for a set of 32 PHAs. Among these, PHA 99942 Apophis is selected for detailed examination, as it holds the highest Torino rating and was sub-

Table 1: The parameters for the spacecraft, low-thrust propulsion system

Parameters	Values
Spacecraft Initial Mass m_0	10,0000kg
Exhaust Velocity c	29.78 kms^{-1}
Initial acceleration n_0	1.7658×10^{-4}ms^{-2}

Table 2: Parameters of 32 PHAs

No	PHA	CA Date	CA distance (km)	$\mathbf{U}$ to Earth (kms^{-1})	Diameter (m)	Rarity
1	Apophis	13 Apr 2029	38012	7.42	0.34±0.04 km	6
2	2019 CD2	1 Feb 1957	75303	19.90	260 m - 590 m	5
3	2001 WN5	26 Jun 2028	248712	10.24	0.932±0.011 km	5
4	2016 EF195	11 Mar 2016	31628	10.09	21 m - 47 m	4
5	Duende	15 Feb 2013	34053	7.82	39 m - 86 m	4
6	2017 QP1	14 Aug 2017	62638	23.96	37 m - 83 m	4
7	2019 OK	25 Jul 2019	71355	24.53	58 m - 130 m	4
8	2012 UE34	8 Apr 2041	109649	6.12	58 m - 130 m	4
9	2017 VW13	8 Nov 2001	143273	11.33	190 m - 430 m	4
10	2005 YU55	8 Nov 2075	203872	13.79	0.4 km	4
11	1998 KJ9	31 Dec 1914	233048	21.10	320 m - 720 m	4
12	2007 YV56	2 Jan 2101	238986	19.28	170 m - 370 m	4
13	2005 WY55	28 May 2065	332741	18.60	190 m - 430 m	4
14	2002 CU11	30 Aug 1925	346943	26.48	0.460±0.017 km	4
15	2011 MD5	17 Sep 1918	350000	12.99	720 m - 1.6 km	4
16	2021 FT1	23 Mar 2098	89089	19.65	33 m - 75 m	3
17	2008 GD110	23 Apr 1968	91682	9.03	33 m - 75 m	3
18	2010 XW58	10 Dec 1957	60810	7.29	28 m - 62 m	3
19	2019 DP	29 Aug 2017	61250	9.50	26 m - 58 m	3
20	2018 CB	9 Feb 2018	69732	7.27	18 m - 39 m	3
21	2009 DD45	2 Mar 2009	72228	8.82	18 m - 41 m	3
22	2016 QA2	28 Aug 2016	86569	10.27	25 m - 57 m	3
23	2023 NT1	13 Jul 2023	100893	11.27	26 m - 58 m	3
24	2018 NL	29 Jun 2055	116731	8.69	22 m - 49 m	3
25	2002 MN	14 Jun 2002	119995	10.57	51 m - 110 m	3
26	2007 UW1	19 Oct 2129	83983	5.63	77 m - 170 m	3
27	2023 GQ2	17 Nov 2193	287543	21.46	280 m - 630 m	3
28	2014 SM143	23 Oct 2197	140937	17.62	220 m - 500 m	3
29	2011 DV	25 Apr 2120	144553	5.97	200 m - 440 m	3
30	2011 JA	26 Apr 2100	207814	22.84	140 m - 310 m	3
31	2000 WO107	1 Dec 2140	243146	26.02	0.510±0.083 km	3
32	1998 OX4	22 Jan 2148	296225	12.30	160 m - 350 m	3

sequently upgraded to level 4—the current record for the highest rating on the Torino Scale. Next, 1998OX4 is analyzed in detail due to its notably distinct results under the two strategies.

3.4. 99942 Apophis

Apophis is a near-Earth PHA discovered in 2004, this PHA is approximately 370 meters in diameter, and it is potentially the most hazardous object monitored by astronomers. Apophis will make a remarkably close approach (CA) to Earth on 21:46 April 13, 2029 (TDB), with a CA distance of 38,011 km to Earth. This distance is even closer than the orbits of some satellites.

Based on a condition of a 10-year warning period, the optimal deflection trajectory found by the COG and BIP strategies is listed in Table 3. Figure (9) shows the transfer trajectories projected onto the x–y plane of the heliocentric J2000 coordinate system, including the position of the spacecraft at the departure and impact moments. Figure (10) illustrates the time histories of the low-thrust in-plane and out-of-plane angles for both strategies.

Both two strategies yield very similar launch windows; however, the BIP strategy's transfer duration is approximately 8 days shorter than that of COG (the launch is delayed by about 6 days, while the impact occurs about 2 days earlier). Meanwhile, the impulse ΔV applied during Earth departure phase

Table 3: Optimal Trajectory for Deflecting 99942 Apophis Found by both the COG and BIP strategies

	Center of Geometry (COG)	Best Impact Point (BIP)
Launch Date	19th Dec 2020 13:48	25th Dec 2020 22:28
Impact Date	17th Jan 2021 16:14	15th Jan 2021 02:04
Flight Duration	29.10 days	21.15 days
Impulse ΔV	12.34 kms^{-1}	17.02 kms^{-1}
Mass at Impact	6510.53 kg	5585.60 kg
Interception Error	2.35×10^{-5} m	8.18×10^{-3} m
Intercept Angle	12.62°	14.09°
Deflection Distance	5,284.69 km	7,409.46 km

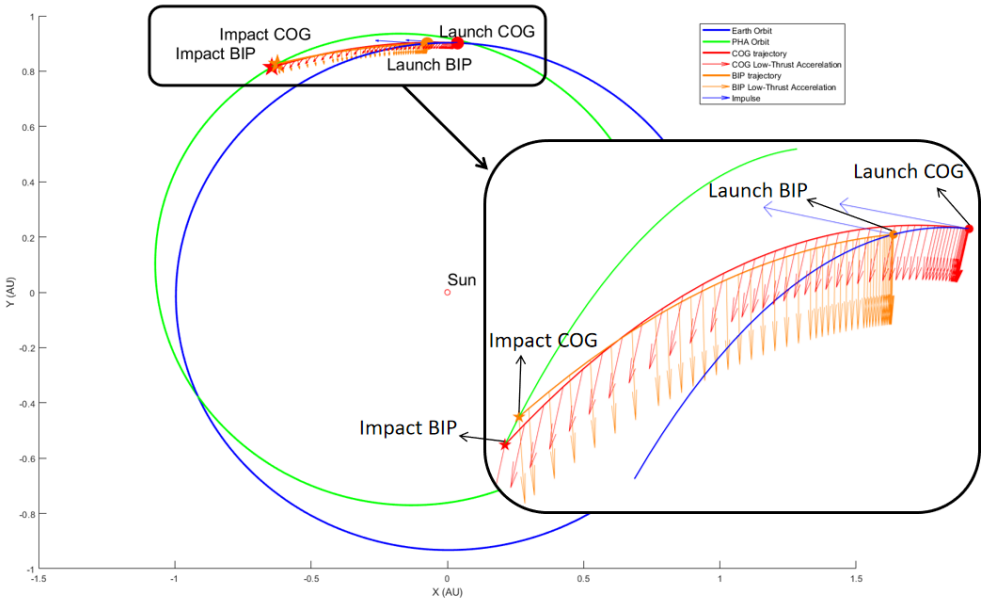

Figure 9: Optimal transfer trajectories for deflecting Apophis found by both the COG (red) and BIP (orange) strategies.

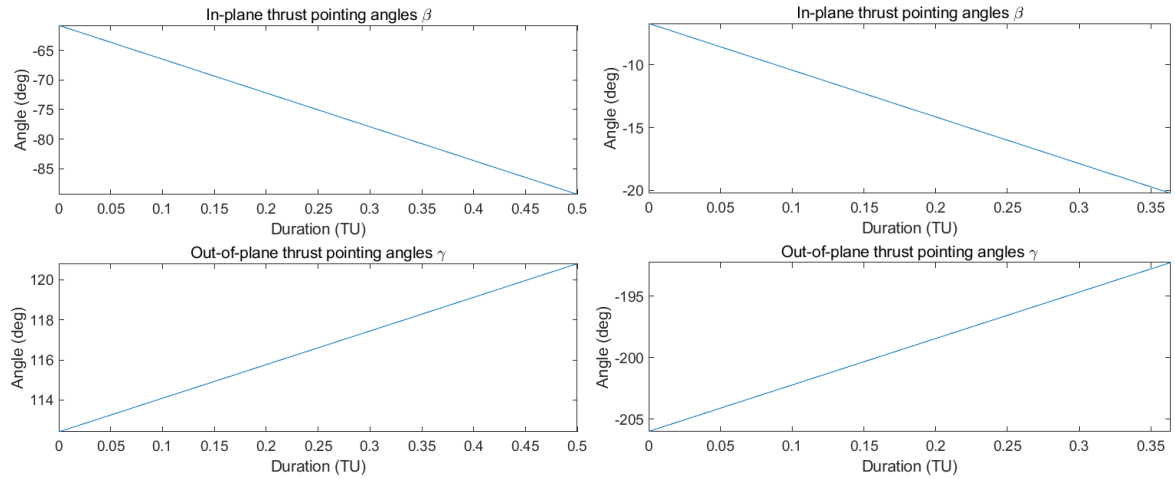

Figure 10: History of in-plane (left) and oOut-of-plane (right) thrust pointing angle during the interception trajectory for Apophis. Where 2πTU $= 365.25$ days

under BIP is roughly $5\,\mathrm{km\,s^{-1}}$ higher than COG, causing the spacecraft mass at impact to be nearly $1000\,\mathrm{kg}$ lower. According to Eqn.(12), the spacecraft mass at impact is directly proportional to the $\delta\mathbf{v}$ imparted to the PHA. Despite sacrificing $1000\,\mathrm{kg}$ of mass, BIP achieves a larger intercept angle, with $\alpha = 14.09°$, compared to $\alpha = 12.62°$ for COG. Consequently, the BIP strategy attains a deflection distance of $7409\,\mathrm{km}$, which represents a 40.21 % increase over the $5284\,\mathrm{km}$ obtained by the COG strategy. This, in turn, further validates our claim.

3.5. 1998 OX4

Although both strategies yield approximately 40 % improvement in the results for the Apophis deflecting mission, their launch windows are extremely similar, and the intercept angles differ only by about 1.5 %. Therefore, in this subsection, we focus on a case with more pronounced differences between the two strategies: Deflecting PHA 1998 OX4.

Based on a condition of a 10-year warning period, the optimal deflection trajectory found by both the COG and BIP strategies is listed in Table 4. Figure (11) shows the transfer trajectories in the heliocentric J2000 coordinate system, including the position of the spacecraft at the departure and impact moments. Figure (12) illustrates the time histories of the low-thrust angles in and out of the plane for both strategies.

Table 4: Optimal trajectory for deflecting 1998 OX4 found by both COG and BIP strategies

	Center of Geometry (COG)	Best Impact Point (BIP)
Launch Date	13th Nov 2139 08:59	4th Jan 2139 02:38
Impact Date	18th Jun 2141 19:33	24th Mar 2141 11:48
Flight Duration	583.44 days	810.38 days
Impulse ΔV	5.50 $\mathrm{kms^{-1}}$	16.70 $\mathrm{kms^{-1}}$
Mass at Impact	6165.55 kg	3768.81 kg
Interception Error	0.3227 m	0.0376 m
Intercept Angle	6.81°	22.56°
Deflection Distance	245.57 km	418.85 km

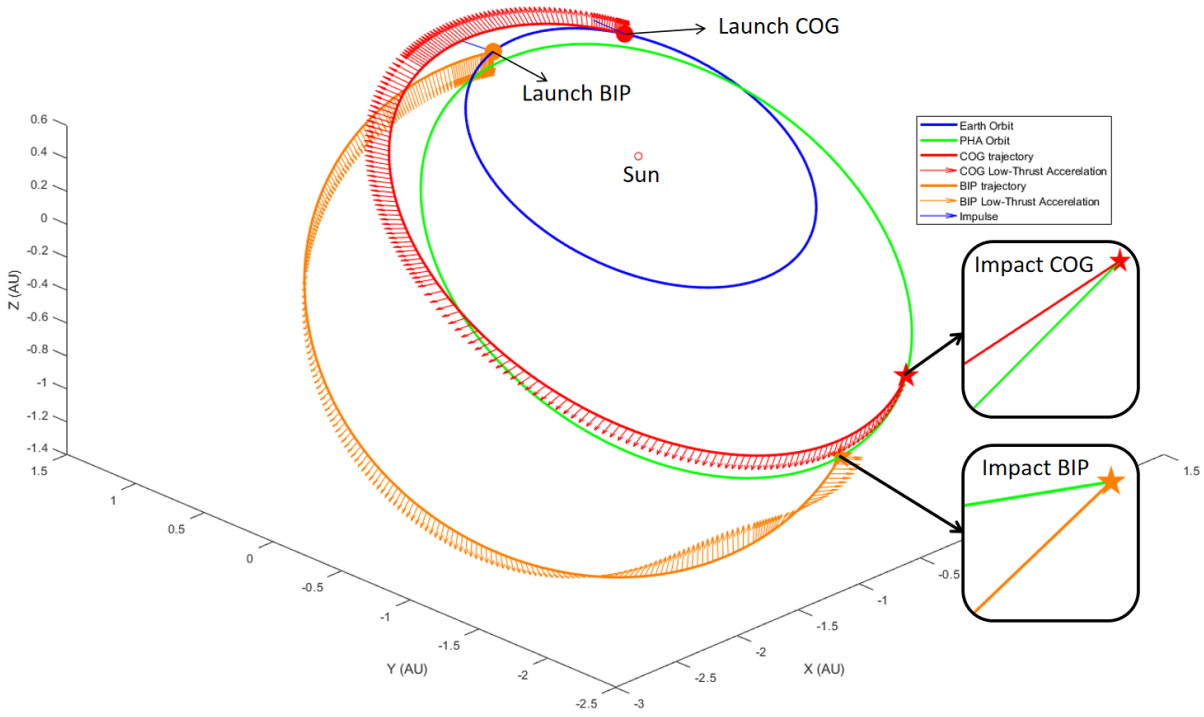

Figure 11: Optimal transfer trajectories for deflecting 1998 OX4 found by both the COG (red) and BIP (orange) Strategies.

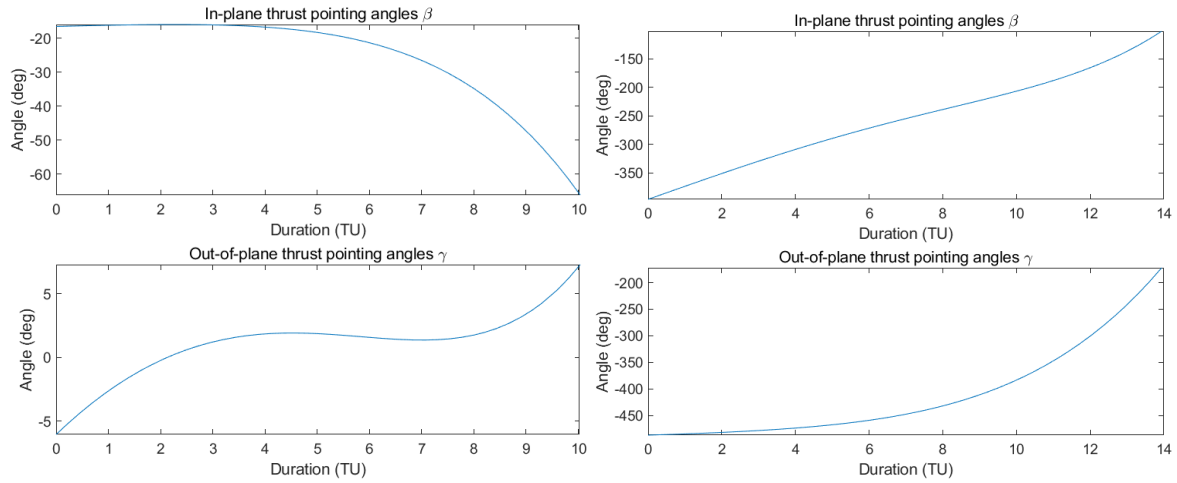

Figure 12: History of in-plane (left) and out-of-plane (right) thrust pointing angle during the interception trajectory for 1998 OX4. Where 2πTU $= 365.25$ days

It can be observed that the transfer trajectory determined by the BIP strategy consumes significantly more fuel than that of the COG strategy, both in terms of the low-thrust transfer phase and the impulse applied during Earth departure phase. Specifically, the impulse is approximately $11\,\mathrm{kms}^{-1}$ higher and the low-thrust transfer duration is extended by about 230 days under the BIP strategy, resulting in a reduction of the spacecraft's mass at impact by roughly 2400 kg compared to the COG strategy. Despite this increased fuel consumption, the BIP strategy achieves a considerably larger interception angle, with $\alpha = 22.56^\circ$ versus $\alpha = 6.81^\circ$ for the COG strategy, ultimately producing a deflection distance of 418 km, an improvement of 70. 61% over the 245 km achieved by the COG strategy. This further validates our initial claim.

3.6. 32 Potentially Hazardous Asteroids PHAs

The simulation results for deflecting 32 PHAs using the COG and BIP strategies are presented in Table 5, and the corresponding transfer trajectories are illustrated in Fig.(13) and Fig.(14). Among these results, PSO under the COG strategy failed to yield a positive deflection distance for two PHAs, namely No.9 (2017 VW13) and No.23 (2023 NT1). This observation is consistent with the Lambert transfer results reported by Lee et al. for these 32 PHAs[3]. Their Lambert launch windows indicate that the deflection of No.23 (2023 NT1) imposes particularly stringent requirements on the PHA's attitude; in their Monte Carlo analysis of 100,000 attitudes samples, nearly 50% produced negative deflection distances under the COG strategy. It is not difficult to surmise that, during the PSO search under the COG strategy, the persistent generation of negative deflection distances prevents the objective function from converging. For No.9 (2017 VW13), the entire Lambert transfer launch window under the COG strategy is negative, corroborating the PSO's inability to obtain a positive deflection distance. In particular, Lee et al. reported eight PHAs failing under the Lambert transfer window of the COG strategy, whereas the combined impulse-low-thrust transfer trajectory approach obtained in this paper reduced the number of failures to two, further validating the efficacy of the combined impulse–low-thrust method for planetary deflection defense missions. Furthermore, although the deflection search fails under the COG strategy for No.9 (2017 VW13) and No.23 (2023 NT1), our proposed BIP strategy is able to achieve positive deflection distances for these PHAs. This further demonstrates the effectiveness of the proposed BIP strategy.

Excluding these two PHAs, for the remaining 30 PHAs, the deflection distances achieved by the BIP strategy are all higher than those obtained with the COG strategy, with an average relative increase of 38.61% and a maximum increase of 177%. This further validates the effectiveness of the proposed BIP strategy. Our initial hypothesis was that incorporating eccentric impact (BIP) would enable the identification of transfer trajectories with interception angles α that were larger than those obtained through the COG strategy, thus further enhancing the deflection distance. Among the 30 PHAs, 26 (87%) exhibited transfer trajectories under the BIP strategy with larger interception angles α than those from the COG strategy, which validates our initial prediction. Despite for 4 PHAs, specifically Nos. 7, 19, 20, and 21 the COG strategy produced higher interception angles α, the resulting deflection distances remained greater under the BIP strategy.

Table 5: Deflecting Simulation Refults for 32 PHAs

		Launch Date		Impact Date		Flight Duration (days)		Impulse ΔV (kms^{-1})		Mass at Impact (t)		Interception Angle (°)		Deflection Distance (km)		
No	PHA	COG	BIP	COG	BIP	COG	BIP	COG	BIP	COG	BIP	COG	BIP	COG	BIP	Gain(%)
1	Apophis	19-12-2020	25-12-2020	17-01-2021	16-01-2021	29.100	21.15	12.34	17.02	6.51	5.59	12.62	14.09	5,285	7,409	40.21
2	2019 CD2	07-01-1950	08-01-1950	10-08-1950	17-06-1950	215.07	159.55	12.49	13.92	5.89	5.77	10.42	10.55	3,803	5,978	57.19
3	2001 WN5	16-07-2019	19-07-2019	05-08-2019	03-08-2019	19.55	15.49	13.83	18.15	6.22	5.39	27.78	38.28	13,412	14,117	5.26
4	2016 EF195	05-03-2008	01-01-2006	10-05-2011	13-10-2006	1161.07	285.38	11.22	7.95	3.61	6.61	21.73	42.94	2,497	6,910	176.69
5	Duende	17-08-2003	15-07-2003	23-08-2003	25-07-2003	5.47	9.48	13.71	17.84	6.29	5.47	4.82	32.35	16,469	19,732	19.81
6	2017 QP1	25-01-2009	14-05-2010	14-04-2009	19-12-2010	78.65	219.38	11.26	15.10	6.58	5.38	34.56	76.97	28,784	31,499	9.43
7	2019 OK	20-01-2011	15-12-2010	25-08-2011	10-08-2011	216.70	238.23	14.60	9.93	5.48	6.34	70.51	65.71	33,275	58,689	76.38
8	2012 UE34	13-09-2033	13-09-2033	31-10-2033	31-10-2033	48.13	48.13	17.93	17.93	5.34	5.34	30.73	30.73	1,826	2,220	21.55
9	2017 VW13	03-01-1993	22-11-1992	31-05-1993	01-06-1993	147.44	190.99	18.56	14.41	4.97	5.59	34.73	30.54	-159	259	-
10	2005 YU55	09-10-2065	05-04-2067	27-10-2070	15-12-2067	1843.95	254.62	0.08	10.93	3.88	6.08	25.25	41.05	15,815	19,720	24.69
11	1998 KJ9	17-06-1907	10-09-1906	15-09-1907	02-09-1907	89.53	357.19	14.14	10.90	5.94	5.78	31.86	56.08	25,789	38,228	48.23
12	2007 YV56	29-09-2092	04-10-2092	30-07-2094	26-08-2093	669.76	325.56	7.59	11.30	5.50	5.79	14.45	20.84	740	803	8.54
13	2005 WY55	27-01-2057	09-03-2056	06-07-2057	10-04-2057	159.93	397.02	2.34	7.88	8.52	6.26	34.08	41.85	30,075	50,679	68.51
14	2002 CU11	31-07-1917	30-07-1917	02-09-1917	28-08-1917	33.07	29.08	17.95	18.29	5.38	5.33	30.69	33.71	3,527	6,321	79.21
15	2011 MD5	19-09-1909	14-09-1909	31-12-1910	29-12-1910	468.42	471.23	9.43	11.21	5.73	5.39	32.07	37.39	1,863	2,349	26.09
16	2021 FT1	16-03-2088	23-03-2088	01-02-2089	01-02-2089	321.60	315.32	1.58	7.41	8.04	6.63	36.26	48.05	44,797	47,856	6.83
17	2008 GD110	18-04-1959	20-05-1958	28-05-1961	22-09-1959	771.31	490.52	7.12	5.01	5.30	6.57	15.08	21.07	32,841	34,768	5.87
18	2010 XW58	09-12-1948	01-01-1947	05-06-1949	24-04-1947	178.16	113.77	11.24	19.80	6.26	4.85	6.07	27.05	2,223	3,485	56.81
19	2019 DP	04-12-2009	24-01-2008	10-10-2010	19-08-2008	310.10	208.47	12.08	10.75	5.69	6.26	39.30	33.20	4,408	5,619	27.47
20	2018 CB	16-05-2011	29-12-2010	11-08-2011	14-02-2011	87.38	47.04	10.48	17.54	6.72	5.41	20.21	19.21	3,489	6,615	89.59
21	2009 DD45	01-01-1999	03-03-1999	30-08-1999	15-10-1999	241.75	226.22	20.00	10.07	4.51	6.35	45.68	28.57	10,736	13,028	21.35
22	2016 QA2	29-08-2006	07-10-2007	29-01-2007	10-02-2008	152.62	125.54	18.84	20.00	4.91	4.79	47.77	66.59	4,195	7,886	87.98
23	2023 NT1	16-01-2013	06-06-2015	29-07-2013	13-09-2018	193.95	1194.63	2.34	7.34	8.37	4.24	20.64	3.34	-695,681	242,650	-
24	2018 NL	04-05-2045	03-06-2045	26-08-2045	18-09-2045	114.13	107.21	14.10	13.47	5.87	6.02	28.50	33.18	15,673	19,105	21.90
25	2002 MN	18-03-1993	27-03-1994	29-07-1994	01-08-1994	498.16	127.57	14.56	20.00	4.75	4.79	26.30	39.52	9,790	13,966	42.66
26	2007 UW1	18-10-2121	29-03-2122	09-11-2122	18-06-2122	387.27	80.31	11.02	12.64	5.66	6.28	22.22	38.20	27,321	31,638	15.80
27	2023 GQ2	11-11-2184	16-11-2184	03-06-2185	02-06-2185	204.31	198.75	9.35	11.03	6.58	6.24	33.18	52.31	241,240	250,013	3.64
28	2014 SM143	05-04-2188	13-04-2188	01-11-2188	02-11-2188	209.51	202.90	9.67	11.06	6.50	6.22	45.96	49.85	1,455	1,702	17.04
29	2011 DV	23-10-2110	14-10-2112	11-06-2111	30-03-2113	230.81	167.35	12.19	19.15	5.90	4.83	27.05	49.63	39,983	41,336	3.38
30	2011 JA	30-03-2091	25-03-2091	19-04-2091	17-04-2091	20.15	22.75	14.88	13.44	6.01	6.29	36.64	39.46	9,233	9,752	5.62
31	2000 WO107	07-06-2130	21-06-2132	13-09-2131	16-08-2133	462.67	421.14	7.27	8.35	6.18	6.09	5.54	30.05	2,568	3,083	20.06
32	1998 OX4	13-11-2139	04-01-2139	18-06-2141	24-03-2141	583.44	810.38	5.50	16.70	6.17	3.77	6.81	22.56	246	419	70.56

It is worth noting that for No.8 (2012 UE34), the two strategies yield nearly identical intercept trajectories, with their launch windows differing by only a few minutes and their interception angles both being approximately 30.73°. Under such an intercept trajectory, the deflection distance achieved by the BIP strategy is 21.55% greater than that of the COG strategy, with deflection distance being 2,2200 km and 1,826 km. This comparison under nearly the same intercept trajectories serves as a compelling demonstration of the performance gains afforded by the BIP strategy.

4. Conclusion

This work has presented a new trajectory optimization framework for kinetic impact asteroid deflection missions by incorporating an eccentric impact strategy, called the Best Impact Point (BIP), within an impulsive-low-thrust combined trajectory design. Traditional trajectory optimizers that aim to maximize the deflection distance typically yield optimal transfer trajectories with intercept angles α being as small as possible. Our team claims that incorporating an eccentric collision strategy into the trajectory optimizer, it will loosen this constraint. We predict that the optimizer will identify intercept trajectories with larger intercept angles α, which could not be found by the traditional optimizer, resulting in greater deflection distances than those obtained by traditional methods. Extensive simulations on 32 potentially hazardous asteroids (PHAs) confirm our claim that all of the intercept tranjectory found by our optimizer ended up with a greater deflection distance than the traditional optimizer.

The primary insight comes from leveraging the increased normal component of ejecta momentum. Unlike conventional schemes that minimize the intercept angle α, which will maximize $\text{proj}_{\mathbf{v}_{\text{ast}}}\delta\mathbf{v}$, the BIP strategy maximizes the component of ejecta velocity change in the orbital velocity direction of the asteroid $\text{proj}_{\mathbf{v}_{\text{ast}}}\mathbf{P}_{\text{ej,n}}$, by exploiting off-center collision geometries. Although this approach may usually require higher fuel consumption to obtain a larger interception angle α, it ultimately produces larger deflection distance relative to Earth.

The results show that for all PHAs considered, the BIP strategy provides markedly higher deflection distances than the conventional COG approach, with an average gain of 38.61%, and up to 170%. These findings highlight that the eccentric impact strategy can measurably enhance momentum transfer under practical mission constraints, thus improving planetary defense outcomes. For specifically No. 9 (2017 VW13) and No. (2023 NT1) which PSO under the COG strategy fails to find a transfer intercept trajectory with positive deflection distance, but PSO under the BIP strategy is able to obtain a positive deflection distance. This demonstrates the effectiveness of the proposed BIP strategy. Finally, 26 of 30 intercept trajectories found by the BIP strategy have a larger interception angle α than the COG strategy; this is consistent with our team's initial predictions.

In summary, this study demonstrates that a larger interception angle α and eccentric impacts significantly increase the efficiency of asteroid kinetic deflection. Future planetary defense initiatives may therefore profit from deliberately foregoing the near-zero intercept angle assumption in favor of more

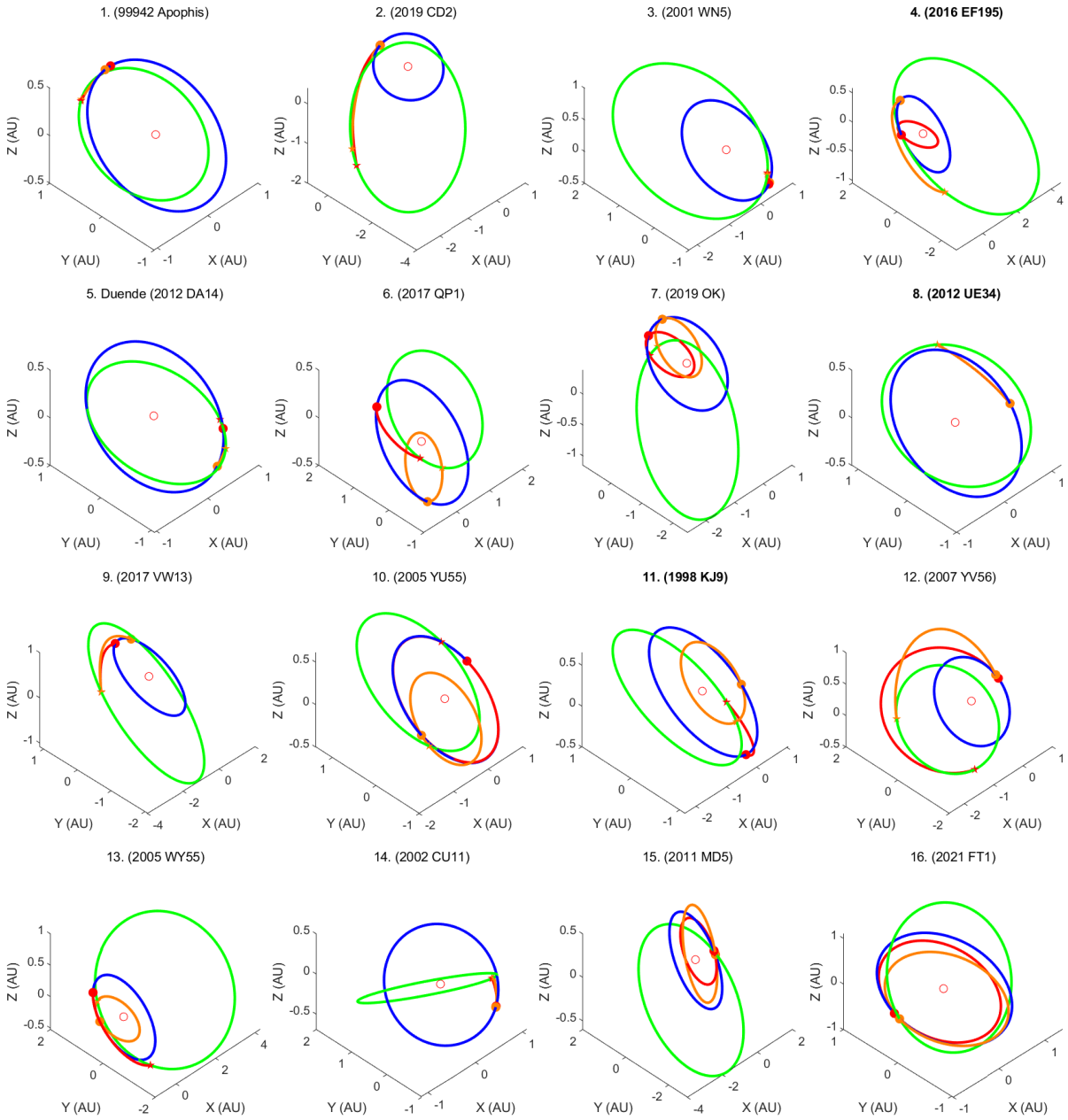

Figure 13: Launch trajectory for the PHAs No.1 to No.16, with the Earth orbit (blue), PHA orbit (green), transfer trajectory obtain by both COG (red) and BIP (orange), filled circle represents launch point, filled star represents intercept point, and the emtpy red circle represents the Sun

eccentric collisions. This study provides important theoretical support and technical reserves for future asteroid defense strategies.

Acknowledgment

This work is supported by the National Natural Science Foundation of China under Grant No.12373066.

References

[1] M. Rebolledo-Vieyra, L. E. Marin, A. Trejo-García, V. L. Sharpton, The chicxulub impact crater and its influence on the regional hydrogeology in northwest yucatan, mexico, Gulf of Mexico origin, waters, and biota. Texas A&M University Press, Killeen, TX (2011) 279–290.

[2] N. Schmidt, Planetary defense governance: Thirty years of development and the multilateral future, Acta Astronautica 214 (2024) 343–355.

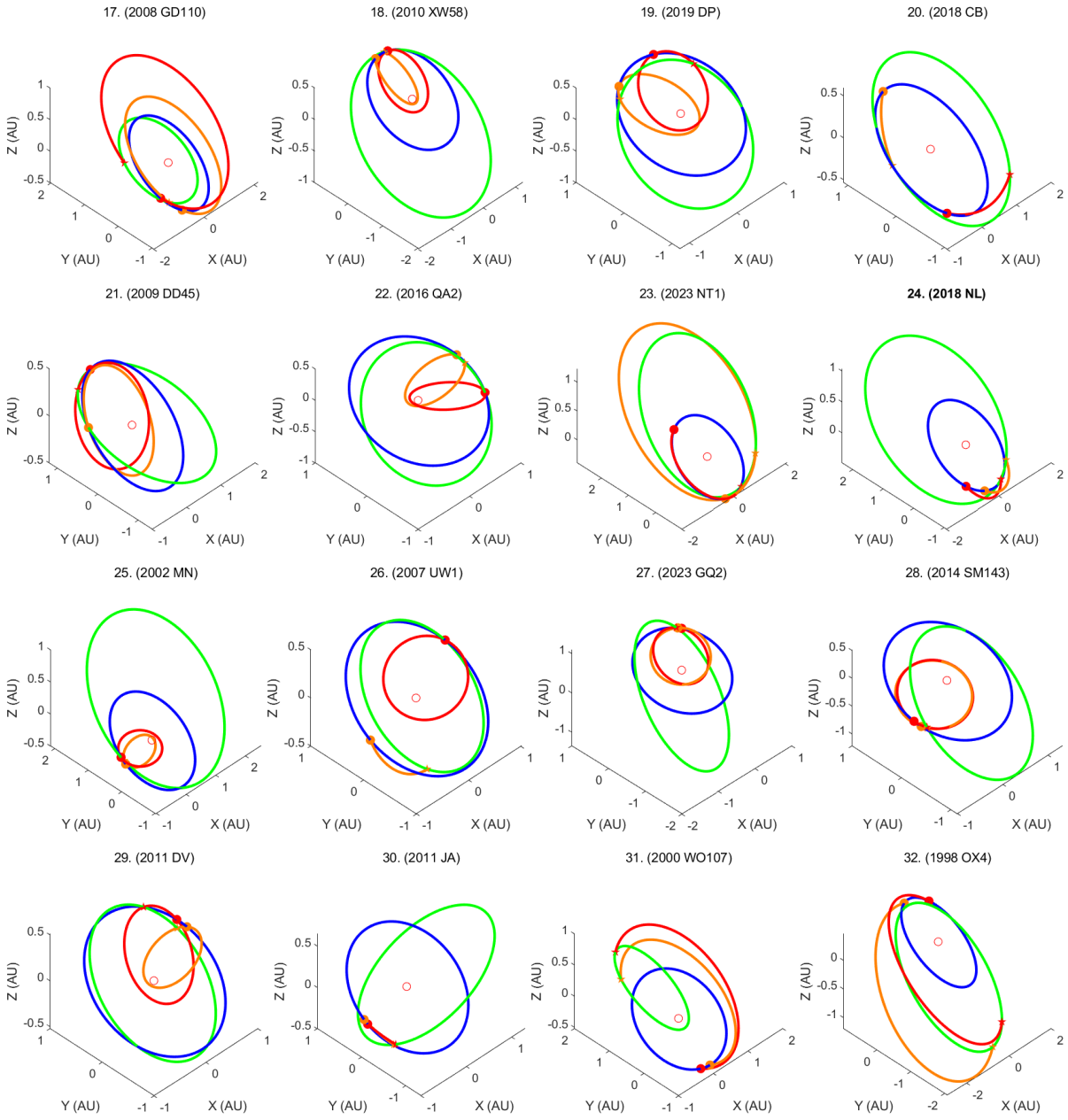

Figure 14: Launch trajectory for the PHAs No.17 to No.32, with the Earth orbit (blue), PHA orbit (green), transfer trajectory obtain by both COG (red) and BIP (orange), filled circle represents launch point, filled star represents intercept point, and the emtpy red circle represents the Sun

[3] K. Lee, Z. Fang, Z. Wang, Investigation of the incremental benefits of eccentric collisions in kinetic deflection of potentially hazardous asteroids, Icarus 425 (2025) 116312.

[4] B. W. Barbee, M. B. Syal, D. Dearborn, G. Gisler, K. Greenaugh, K. M. Howley, R. Leung, J. Lyzhoft, P. L. Miller, J. A. Nuth, et al., Options and uncertainties in planetary defense: Mission planning and vehicle design for flexible response, Acta Astronautica 143 (2018) 37–61.

[5] A. Domínguez, V. M. Moreno, F. Cabral, Kinetic impactor for a short warning asteroid deflection, Acta Astronautica 202 (2023) 791–798.

[6] C. Bombardelli, H. Urrutxua, M. Merino, J. Pelaez, E. Ahedo, The ion beam shepherd: A new concept for asteroid deflection, Acta Astronautica 90 (2013) 98–102.

[7] C. Bombardelli, E. J. Calero, J. L. Gonzalo, Deflection of fictitious asteroid 2017 pdc: Ion beam vs. kinetic impactor, Acta Astronautica 156 (2019) 301–307.

[8] D. Robertson, L. Wheeler, D. Mathias, Evacuation and shelter plans for asteroid impacts informed by hurricanes and nuclear explosions, Acta Astronautica 215 (2024) 739–755.

[9] M. B. Syal, D. S. Dearborn, P. H. Schultz, Limits on the use of nuclear explosives for asteroid deflection, Acta Astronautica 90 (2013) 103–111.

[10] A. S. Rivkin, N. L. Chabot, A. M. Stickle, C. A. Thomas, D. C. Richardson, O. Barnouin, E. G. Fahnestock, C. M. Ernst, A. F. Cheng, S. Chesley, et al., The double asteroid redirection test (dart): Planetary defense investigations and requirements,

The Planetary Science Journal 2 (2021) 173.
[11] R. T. Daly, C. M. Ernst, O. S. Barnouin, N. L. Chabot, A. S. Rivkin, A. F. Cheng, E. Y. Adams, H. F. Agrusa, E. D. Abel, A. L. Alford, et al., Successful kinetic impact into an asteroid for planetary defence, Nature 616 (2023) 443–447.
[12] Y. Zhang, P. Michel, D. C. Richardson, O. S. Barnouin, H. F. Agrusa, K. Tsiganis, C. Manzoni, B. H. May, Creep stability of the dart/hera mission target 65803 didymos: Ii. the role of cohesion, Icarus 362 (2021) 114433.
[13] A. F. Cheng, H. F. Agrusa, B. W. Barbee, A. J. Meyer, T. L. Farnham, S. D. Raducan, D. C. Richardson, E. Dotto, A. Zinzi, V. Della Corte, et al., Momentum transfer from the dart mission kinetic impact on asteroid dimorphos, Nature 616 (2023) 457–460.
[14] M. Vasile, C. Colombo, Optimal impact strategies for asteroid deflection, Journal of guidance, control, and dynamics 31 (2008) 858–872.
[15] S.-D. Raducan, T. Davison, G. Collins, Ejecta distribution and momentum transfer from oblique impacts on asteroid surfaces, Icarus 374 (2022) 114793.
[16] M. Yanagisawa, S. Hasegawa, Momentum transfer in oblique impacts: Implications for asteroid rotations, Icarus 146 (2000) 270–288.
[17] J. L. Anderson, P. H. Schultz, J. T. Heineck, Experimental ejection angles for oblique impacts: Implications for the subsurface flow-field, Meteoritics & Planetary Science 39 (2004) 303–320.
[18] P. Pravec, P. Scheirich, J. Ďurech, J. Pollock, P. Kušnirák, K. Hornoch, A. Galad, D. Vokrouhlickỳ, A. Harris, E. Jehin, et al., The tumbling spin state of (99942) apophis, Icarus 233 (2014) 48–60.
[19] B. A. Conway, A. Speziale, L. Malagni, Optimal combined impulsive/low-thrust trajectories for asteroid deflection via kinetic impact, Acta Astronautica 220 (2024) 516–524.
[20] R. Eberhart, J. Kennedy, A new optimizer using particle swarm theory, in: MHS'95. Proceedings of the sixth international symposium on micro machine and human science, Ieee, pp. 39–43.
[21] M. Pontani, B. A. Conway, Swarming theory applied to space trajectory optimization, in: Spacecraft Trajectory Optimization, Cambridge University Press, 2010, pp. 263–294.
[22] B. A. Conway, A survey of methods available for the numerical optimization of continuous dynamic systems, Journal of Optimization Theory and Applications 152 (2012) 271–306.
[23] R. Chai, A. Savvaris, A. Tsourdos, S. Chai, Y. Xia, A review of optimization techniques in spacecraft flight trajectory design, Progress in aerospace sciences 109 (2019) 100543.
[24] A. M. Stickle, K. M. Kumamoto, D. M. Graninger, M. E. DeCoster, W. K. Caldwell, J. M. Pearl, J. M. Owen, O. Barnouin, G. S. Collins, R. T. Daly, et al., Dimorphos's material properties and estimates of crater size from the dart impact, The Planetary Science Journal 6 (2025) 38.
[25] F. Ferrari, P. Panicucci, G. Merisio, C. Giordano, M. Pugliatti, J.-Y. Li, E. G. Fahnestock, S. D. Raducan, M. Jutzi, S. Soldini, et al., Morphology of ejecta features from the impact on asteroid dimorphos, Nature Communications 16 (2025) 1601.
[26] M. Hirabayashi, S. D. Raducan, J. M. Sunshine, T. L. Farnham, J. Deshapriya, J.-Y. Li, G. Tancredi, S. R. Chesley, R. T. Daly, C. M. Ernst, et al., Elliptical ejecta of asteroid dimorphos is due to its surface curvature, Nature Communications 16 (2025) 1602.
[27] NASA/JPL Center for Near-Earth Object Studies, Close approaches, `https://cneos.jpl.nasa.gov/ca/`, 2024. Accessed: 2024-05-08.